CHAPTER EIGHT

Planar Dynamic Modeling and Analysis

8.1 MODELING AND ANALYSIS TECHNIQUES

Modeling the dynamics of a planar machine involves selecting a kinematic model; defining the initial conditions, forces, and inertia properties of components of the system; and forming and solving the equations of motion. Three fundamentally different modes of dynamic analysis may be considered; (1) *equilibrium analysis,* in which an equilibrium position is sought under the action of specified forces, (2) *inverse dynamic analysis,* in which drivers define the motion of the system and reaction forces are calculated from Lagrange multipliers, and (3) *dynamic analysis,* in which transient response to applied forces is predicted by integrating the mixed differential–algebraic equations of motion.

The results of a dynamic analysis depend on the inertia properties of a system, as well as on the kinematic model selected. If composite joints, called massless links, are employed in analysis, the engineer must be aware that the mass properties of the couplers are being neglected. In many cases, the mass of a coupler can be distributed as lumped masses at the attachment points on each of the bodies that are connected. This procedure can improve the quality of approximation, but will not be precisely equivalent to results that are obtained by defining the actual mass distribution of the coupler.

It is important that data be generated that are consistent with the conventions used in Chapter 6 to derive the governing equations of motion. In particular, the origin of each body-fixed x'-y' frame must be at the center of mass of the body. Otherwise, fundamental errors will be made in the resulting dynamic predictions. Furthermore, the force and torque system that acts on each body from external sources must be reduced to a force that acts at the center of mass of the body and an associated torque.

The same examples studied kinematically in Chapter 5 are analyzed in this chapter with the aid of the DADS computer code [27]. All data required to formulate the equations of motion derived in Chapter 5 are given in tabular

form. These data and kinematic data for the models presented in Chapter 5 are entered into the DADS computer code. The governing equations of motion are automatically formed and solved in the DADS code, which implements the numerical methods presented in Chapter 7. The focus of this chapter is on problem formulation and interpretation of results.

While the analytical techniques presented in the preceding chapters can be effectively learned in a classroom or in self-study, the development of a practical capability in dynamic system modeling and analysis requires considerable application experience. The engineer or engineering analyst must develop intuition that is based on experience in order to evaluate results that are predicted by either a general-purpose computer code such as DADS or by a special-purpose computer program. Even with a well-tested, error-free, general-purpose computer code, if the user makes errors in input data or defines a poor design, undesired behavior of the system will occur. The engineer must thus develop a qualitative understanding of machine dynamics in order to evaluate the reasonableness of the results and to modify a design to improve its dynamic performance.

Examples presented in this chapter are intended to assist the engineer in developing a practical capability in problem formulation and analysis of results. There is no substitute, however, for hands-on experience. Project-oriented problems are given in the problem set at the end of the chapter. It is recommended that the reader obtain access to a general-purpose machine dynamics computer code, such as DADS, and gain experience through the systematic analysis of systems of his or her own design. Critical evaluation of analysis results and study of the effect of alternative models and parameter variations (e.g., dimension changes, mass changes, and force changes) can provide valuable insights and a qualitative understanding of machine dynamics. The value of such experience-based understanding cannot be overestimated.

8.2 DYNAMIC ANALYSIS OF A SLIDER–CRANK MECHANISM

8.2.1 Dynamic Modeling

The dynamic model of a slider–crank mechanism used here for illustration is based on model 1 of Section 5.2.1. Kinematic joint data are the same as provided in Section 5.2.1, with the dimensions in Tables 5.2.1 and 5.2.2 given in units of meters.

Centers of mass of the bodies are at the origins of the body-fixed reference frames in Fig. 5.2.1. Mass and inertia of the ground body are taken as unit quantities, which is unimportant since this body is rigidly connected to the inertial reference frame. Masses and moments of inertia of the four bodies that make up the model are given in Table 8.2.1.

TABLE 8.2.1 Inertia Properties of Slider–Crank

Body no.	1	2	3	4
Mass (kg)	200.0	35.0	25.0	1.0
Moment of inertia (kg · m^2)	450.0	35.0	0.02	1.0

If the slider–crank functions as a compressor, the slider moves in the compression chamber, as shown in Fig. 8.2.1. As the slider moves to the right, a resisting force due to compression of gas acts on the slider. This force increases until the exhaust valve opens. Figure 8.2.2 defines gas force F_c on the slider, as a function of position and velocity of the slider. During the compression stroke of the slider, that is, when $\dot{x}_3 > 0$,

$$F_c = \begin{cases} -\dfrac{282{,}857}{6 - x_3} + 62{,}857, & 1.5 \leq x_3 \leq 5 \\ -110{,}000[1 - \sin 2\pi(x_3 - 5.25)], & 5 < x_3 \leq 5.5 \end{cases}$$

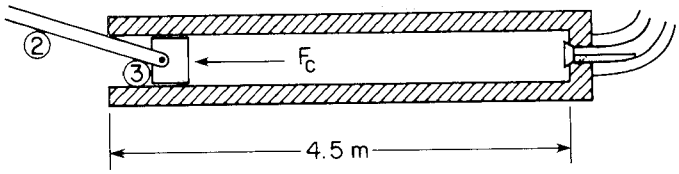

Figure 8.2.1 Slider in a compression gas chamber.

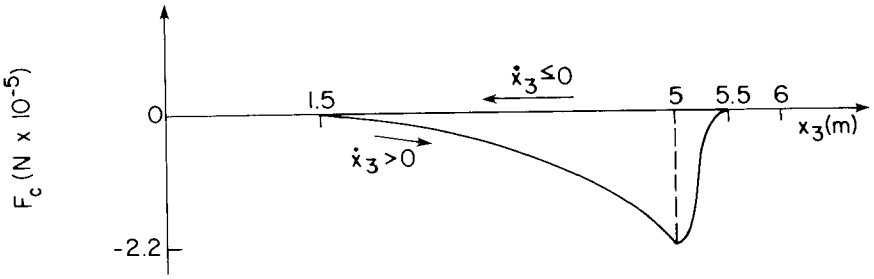

Figure 8.2.2 Gas force versus slider position.

When $x_3 = 5$ m, the valve opens. During the intake stroke of the slider; that is, when $\dot{x}_3 \leq 0$, no force acts on the slider.

8.2.2 Equilibrium Analysis

Gravity is taken as acting in the negative y direction. If gravitational force is the only force that acts on the system, then the equilibrium configuration is expected

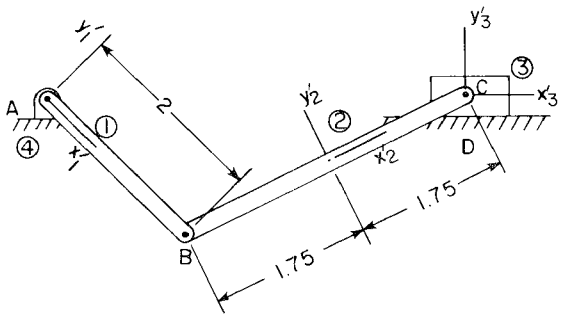

Figure 8.2.3 Estimated equilibrium position.

to be of the form shown in Fig. 8.2.3. An estimate of the equilibrium position used as input is given in Table 8.2.2.

TABLE 8.2.2 Estimated Slider–Crank Equilibrium Position

Body no.	1	2	3	4
x	0.0	1.20	2.67	0.0
y	−0.0	−1.0	0.0	0.0
ϕ	4.6	0.6	0.0	0.0

Equilibrium analysis under only the influence of gravitational force is carried out using the minimum total potential energy method of Section 6.5, with the numerical results presented in Table 8.2.3. Note that the center of mass of the connecting rod is as low as possible, hence minimizing the potential energy of the gravitational force.

TABLE 8.2.3 Slider–Crank Equilibrium Position under Gravitational Force

Body no.	1	2	3	4
x	0.0	1.4635	2.900	0.0
y	0.0	−1.0	0.0	0.0
ϕ	4.726	0.6082	0.0	0.0

If the gas force F_c acts on body 3 in the negative x direction, equilibrium analysis may again be carried out using the minimum total potential energy

TABLE 8.2.4 Slider–Crank Equilibrium Position under Gravitational and Gas Force

Body no.	1	2	3	4
x	0.0	1.2170	2.6575	0.0
y	0.0	−0.9937	0.0	0.0
ϕ	4.6004	0.6039	0.0	0.0

method. Numerical results for this calculation are given in Table 8.2.4. Note that, as expected, body 3 has moved to the left, relative to the position given in Table 8.2.3, and the positions and angles of bodies 1 and 2 are correspondingly changed.

8.2.3 Inverse Dynamic Analysis

The kinematic driving condition prescribed in Section 5.2.3 is used, with the assembled position of Table 5.2.6, to carry out inverse dynamic analysis. Gravitational force is neglected in this analysis. The torque required to achieve the constant angular velocity driving condition and the reaction force at the crank bearing (point A in Fig. 8.2.3) are calculated using Lagrange multipliers, as in Section 6.6, and plotted in Fig. 8.2.4.

8.2.4 Dynamic Analysis

As an illustration of dynamic response analysis, the compressor is analyzed with gravitational force acting in the positive x direction. Motion begins at $t = 0$, with $\phi_1(0) = \pi$ and $\dot{\phi}_1(0) = 30$ rad/s. A constant torque of 41,450 N is applied to the crank, and the force of Fig. 8.2.2 acts on the slider. The applied torque selected does the same amount of work in one revolution as the work done in compressing gas during one cycle, that is, the area under the curve of Fig. 8.2.2. Thus, the compressor should run in steady-state motion.

Three simulations are carried out with different values of polar moment of inertia of the crank, the flywheel in this application: $J_1^1 = 225\ \text{kg} \cdot \text{m}^2$, $J_1^2 = 450\ \text{kg} \cdot \text{m}^2$, and $J_1^3 = 900\ \text{kg} \cdot \text{m}^2$. It is expected that the larger flywheel inertias will lead to less variation in the angular velocity of the flywheel. Plots of angular velocity of the flywheel in Fig. 8.2.5 confirm this behavior. In fact, the smallest inertia J_1^1 leads to failure of the compressor to complete a single cycle. To understand why this happens, note that the work required to compress the gas during the first half-revolution of the flywheel is 260,438 N · m, whereas the sum of the initial kinetic energy of the flywheel and the work done by the applied torque during the same period would be only $225(30^2)/2 + \pi \times 41{,}450 = 231{,}469\ \text{N} \cdot \text{m}$.

Both of the larger moments of inertia of the flywheel provide adequate initial kinetic energy to carry the compressor through a full cycle and to continue

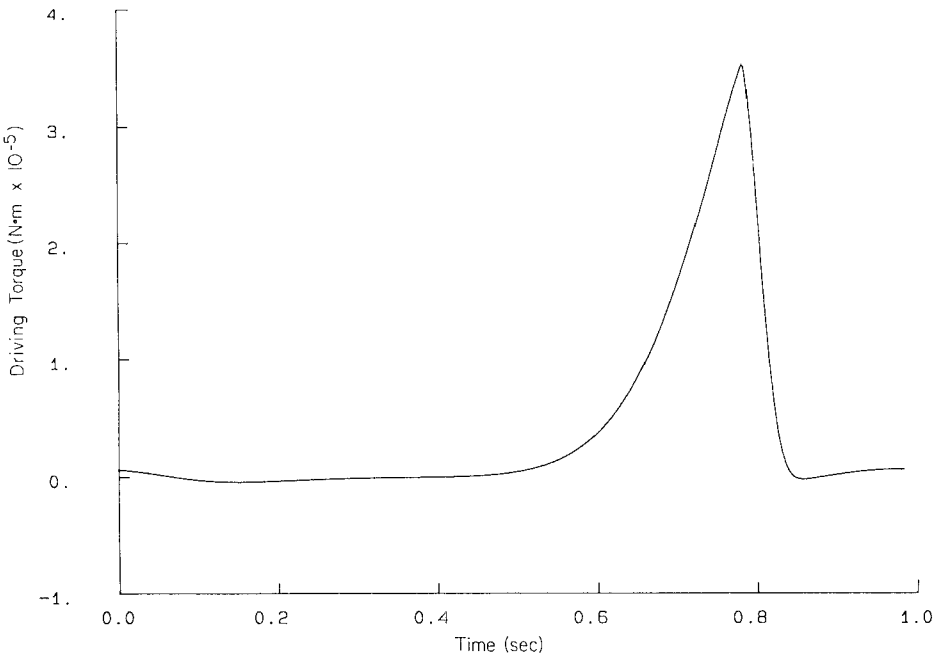

Figure 8.2.4(a) Driving torque: Kinematically driven slider–crank.

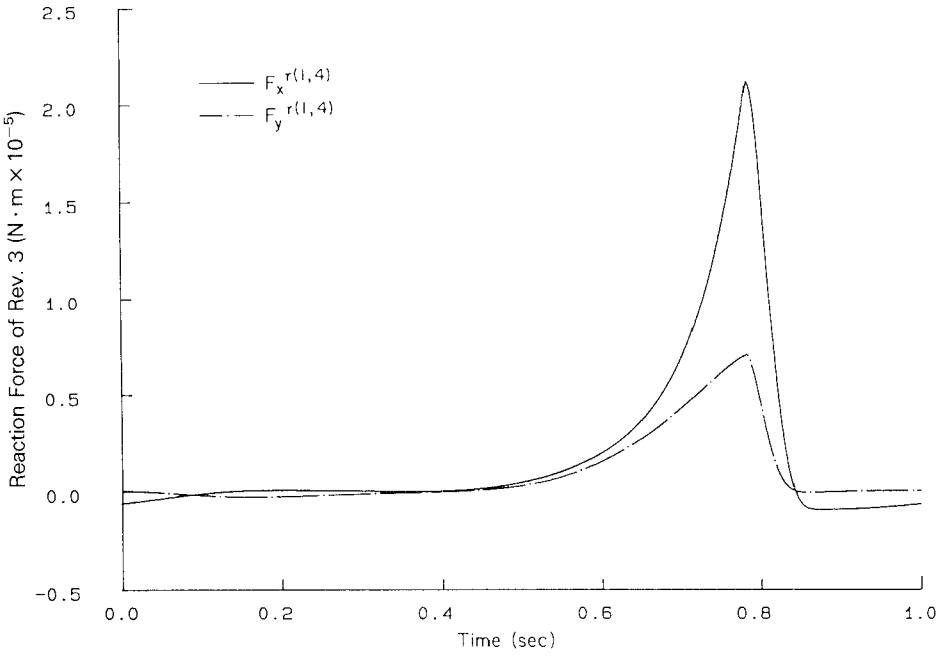

Figure 8.2.4(b) Reaction force: Kinematically driven slider-crank.

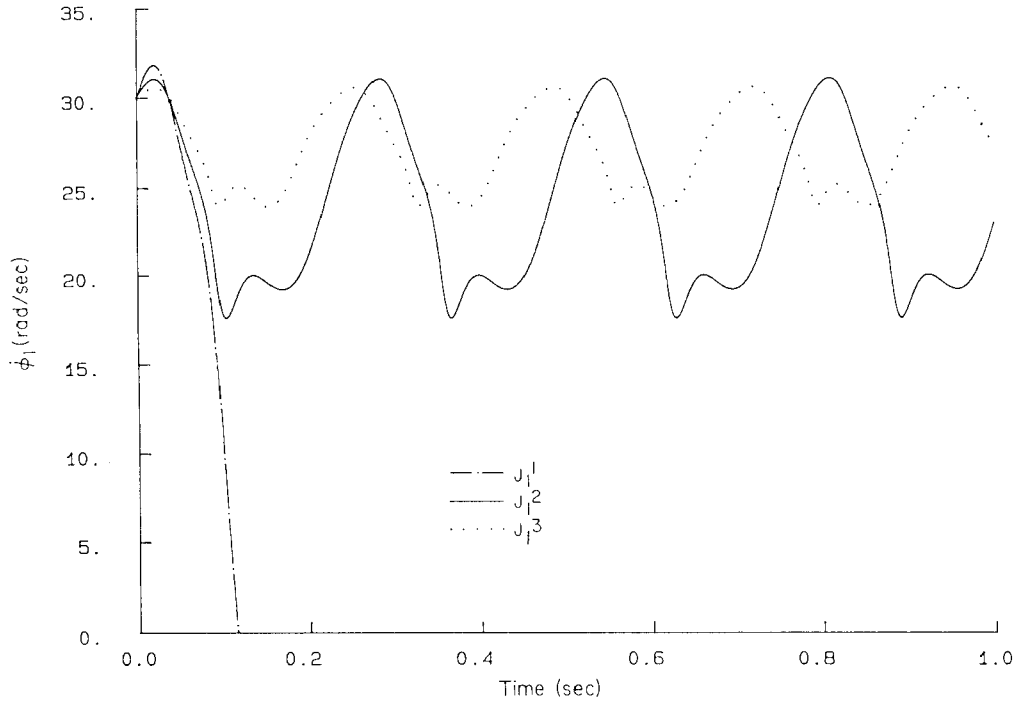

Figure 8.2.5 Angular velocity of flywheel versus time.

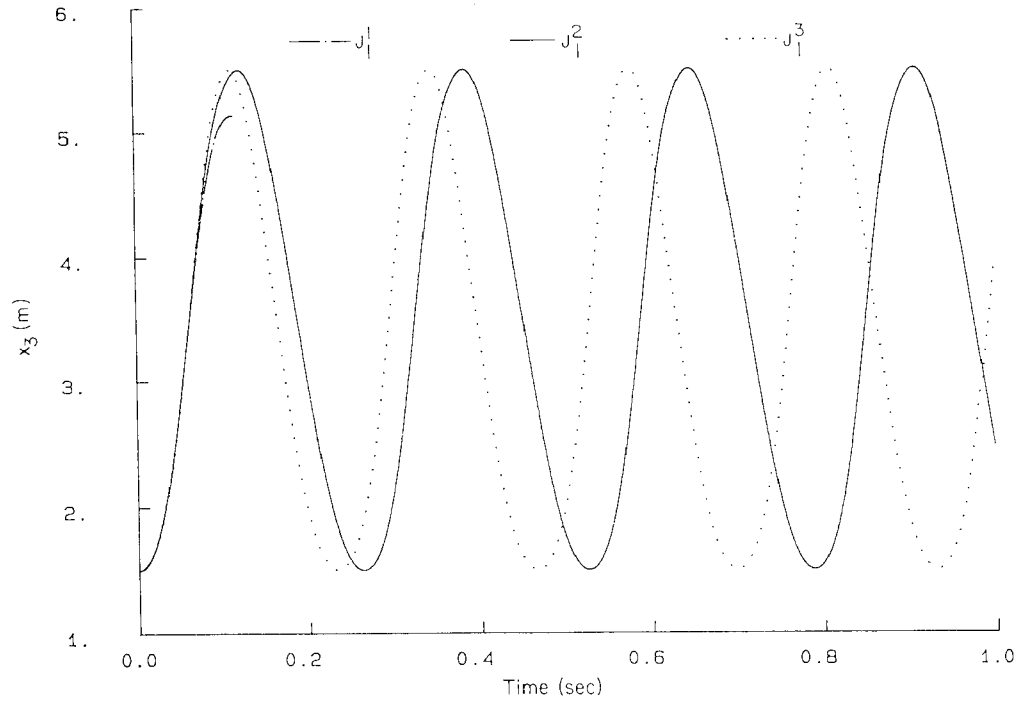

Figure 8.2.6 Position of slider versus time.

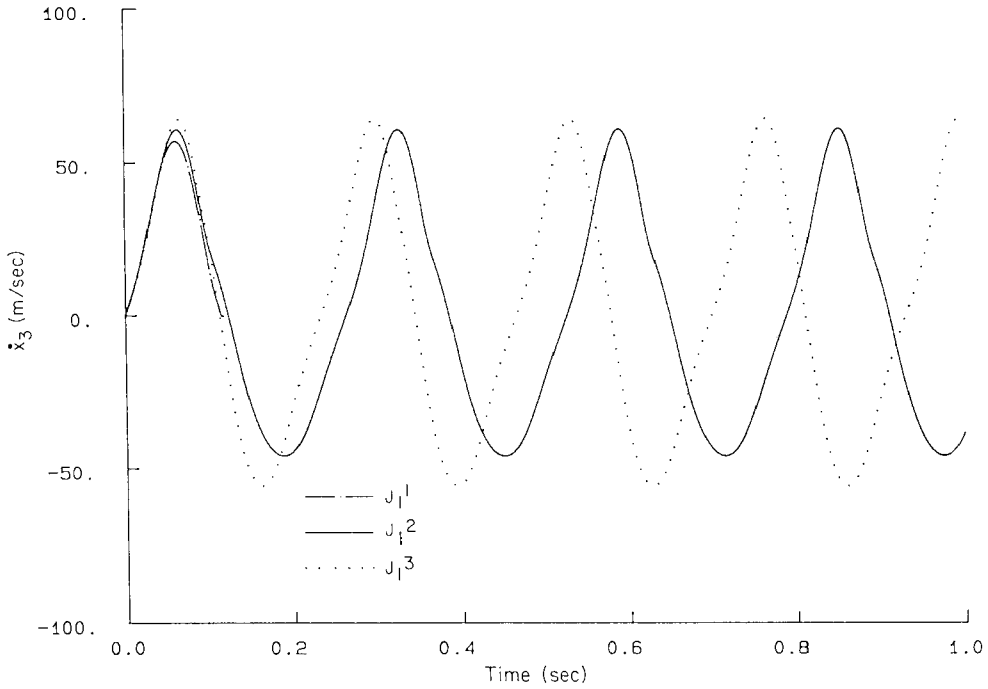

Figure 8.2.7 Velocity of slider versus time.

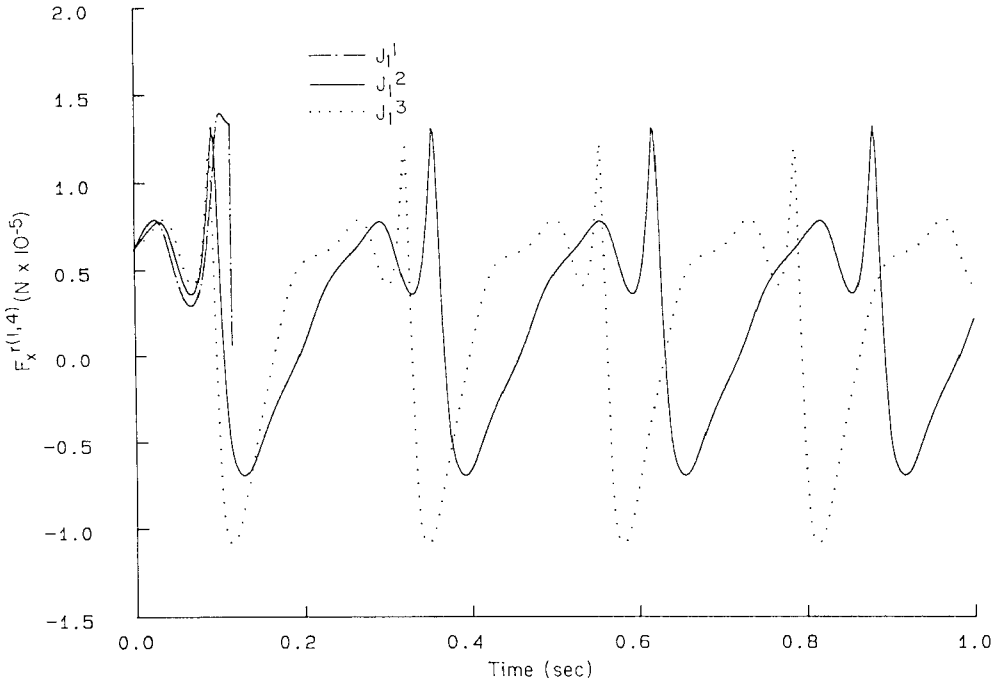

Figure 8.2.8 x-component of reaction force at flywheel bearing versus time.

periodic motion. Note also that the largest flywheel inertia leads to the least variation in flywheel angular velocity, as expected. In fact, from Fig. 8.2.5, the number of compressor cycles per second for J_1^2 and J_1^3 are approximately 3.7 and 4.2 cycles/s, respectively.

Plots of slider position and velocity for each of the flywheel moments of inertia are shown in Figs. 8.2.6 and 8.2.7, respectively. The stroke of the compressor is the same due to identical kinematics. There is a phase shift in velocity, however, due to the difference in flywheel angular velocities. As shown in Fig. 8.2.7, there is also a slight variation in peak slider velocity.

Finally, the x component of reaction force at the flywheel bearing, the revolute joint between bodies 1 and 4, is plotted versus time in Fig. 8.2.8. The more vigorous action of the flywheel with largest inertia leads to a slightly larger variation in reaction force, as might have been expected.

8.3 DYNAMIC ANALYSIS OF A QUICK-RETURN MECHANISM

8.3.1 Dynamic Modeling

The kinematic model 1 of Section 5.4.1 is used here to study the dynamics of the quick-return mechanism of Fig. 5.4.1, which functions as a shaper (see Fig. 1.1.8). A counterclockwise torque is applied to the driving link, body 3. The force between the tool and workpiece required to remove material is given as a function of slider position in Fig. 8.3.1, for the cutting stroke, that is, when $\dot{x}_6 < 0$. When $\dot{x}_6 > 0$, the cutting force is zero. Masses and moments of inertia of the components of the model are presented in Table 8.3.1.

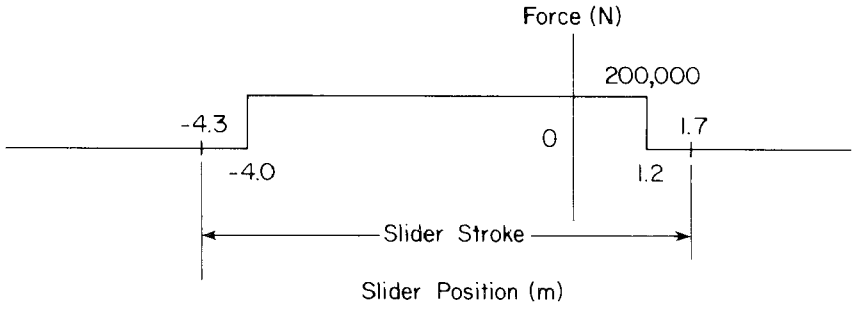

Figure 8.3.1 Cutting force versus slider position.

TABLE 8.3.1 Inertia Properties of Quick-Return Mechanism

Body no.	1	2	3	4	5	6
Mass (kg)	1.0	100.0	1000.0	5.0	30.0	50.0
Moment of inertia (kg · m^2)	1.0	100.0	2000.0	0.05	10.0	1.5

8.3.2 Equilibrium Analysis

With only gravitational force acting in the negative y direction, the equilibrium position of the system might be expected to have body 2 rotated somewhat clockwise from the position shown in Fig. 5.4.1. Equilibrium analysis under gravitational loading only is carried out, using the position estimates provided in Table 5.4.5. The resulting equilibrium configuration is given in Table 8.3.2. As expected, the angle of orientation of body 3 is in the fourth quadrant, and body 2 is rotated clockwise toward the horizontal position.

TABLE 8.3.2 Equilibrium Position of Quick-Return Mechanism under Gravitational Load

Body no.	1	2	3	4	5	6
x	0.0	1.4998	0.0	0.97196	2.3329	1.6663
y	0.0	1.3232	2.0	0.85750	3.3232	4.0
ϕ	0.0	0.72292	−0.86588	0.72292	−0.79302	0.0

8.3.3 Inverse Dynamic Analysis

Inverse dynamic analysis is carried out with a constant angular velocity $\dot{\phi}_3 = 2\pi$ rad/s of the crank, or flywheel. The simulation starts immediately after the cutting stroke; that is, when the slider position is $x_6 = -4.0$ m. Three simulations are carried out, with slider masses $m_6^1 = 25$ kg, $m_6^2 = 50$ kg, and $m_6^3 = 100$ kg. Driving torques that are required to maintain the specified angular velocity of the flywheel are shown in Fig. 8.3.2. Note that the only significant variations in driving torque occur during the period just prior to the cutting stroke, when the slider velocity must be changed from negative to positive (i.e., at the left extreme of the slider stroke).

8.3.4 Dynamic Analysis

Dynamic analysis is carried out with a slider mass $m_6 = 50$ kg, a torque $T_3 = 165{,}521$ N · m applied to the flywheel, and flywheel polar moments of inertia $J_3^1 = 1000$ kg · m^2, $J_3^2 = 2000$ kg · m^2, and $J_3^3 = 4000$ kg · m^2. The applied torque is selected so that the work done in one cycle of operation ($2\pi T_3$) is equal to the work done in cutting the workpiece (the area under the curve of Fig. 8.3.1, 10.4×10^5 N · m).

Plots of slider position and flywheel angular velocity versus time are given in Figs. 8.3.3 and 8.3.4. As expected, the variation in flywheel angular velocity is least for the largest polar moment of inertia. The slider strokes are equal, but phase changes occur due to variations in average angular velocities. The cyclic rates of the shaper, with J_3^1, J_3^2, and J_3^3, are approximately 2.2, 1.8, and 1.5 cycles/s, respectively. It is interesting that in this example the largest flywheel

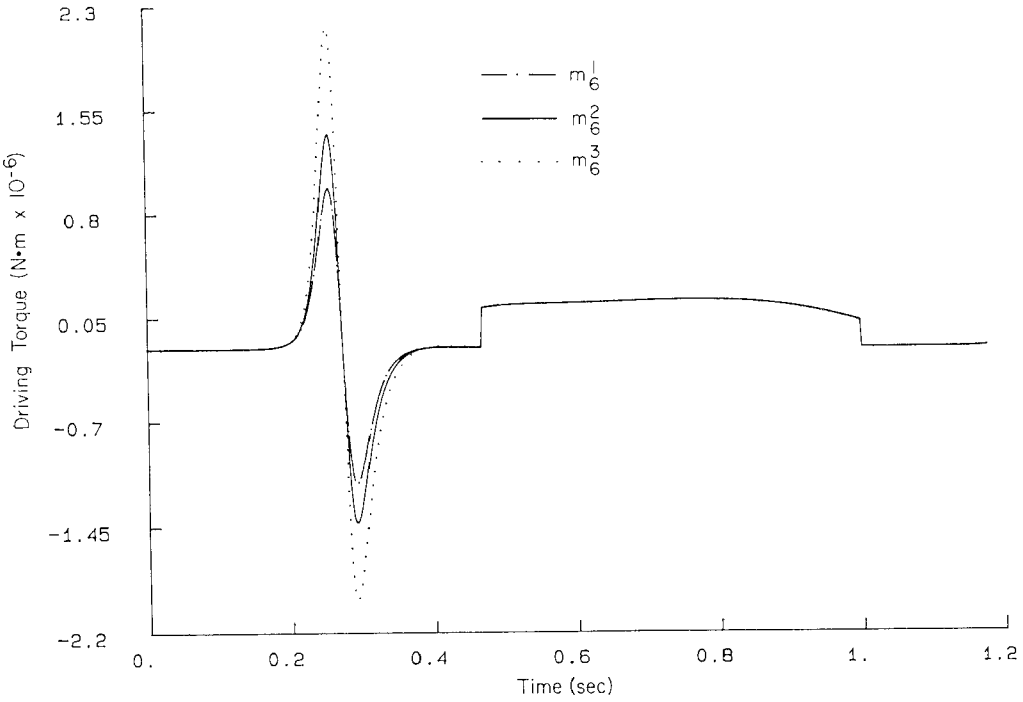

Figure 8.3.2 Driving torque versus time.

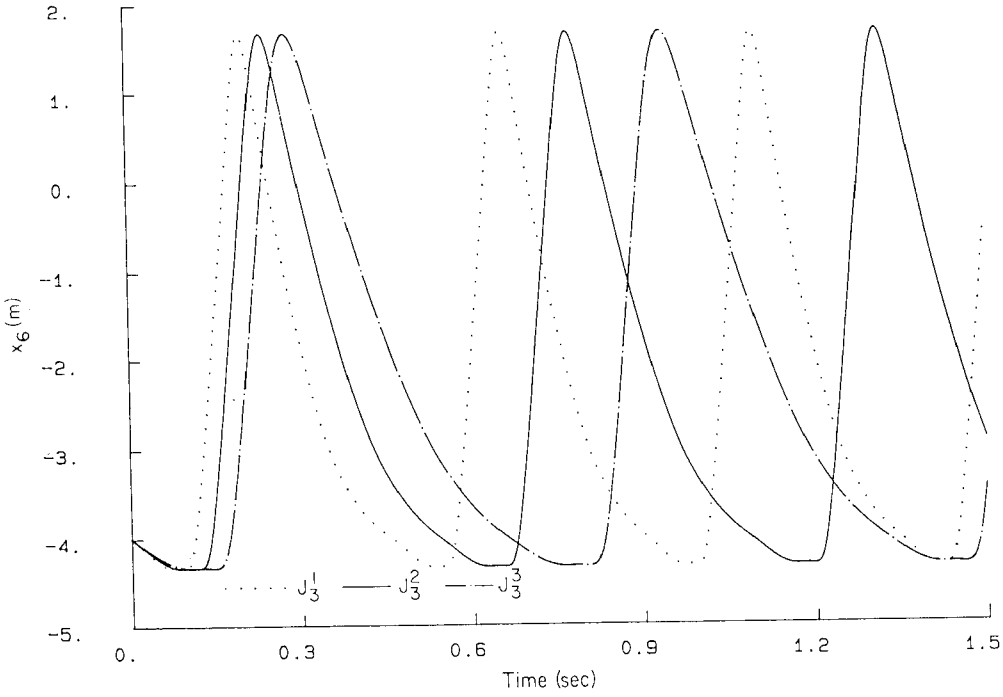

Figure 8.3.3 Slider position versus time.

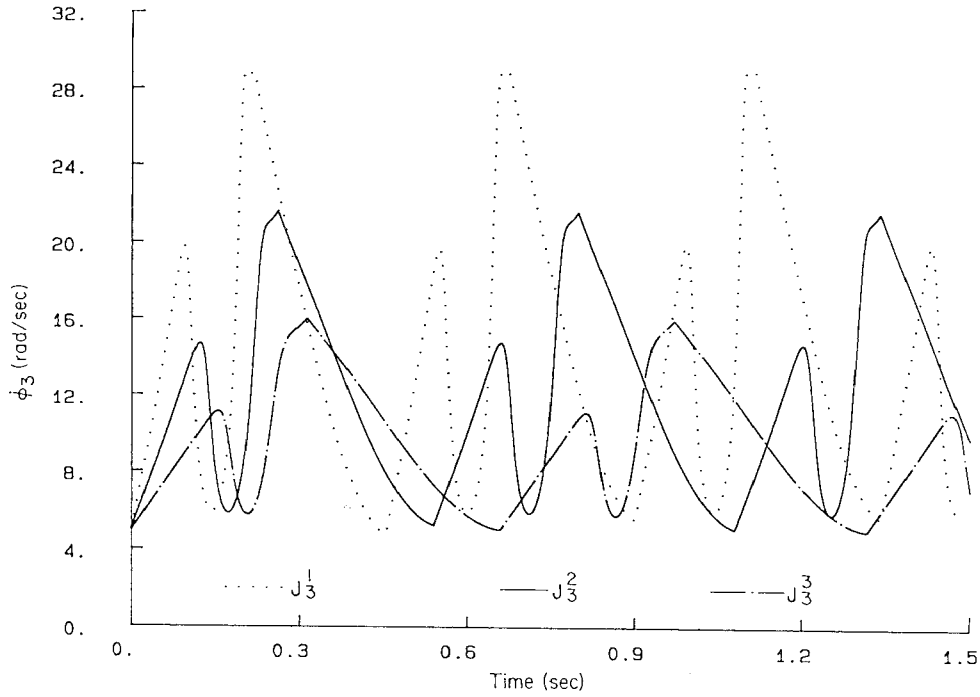

Figure 8.3.4 Flywheel angular velocity versus time.

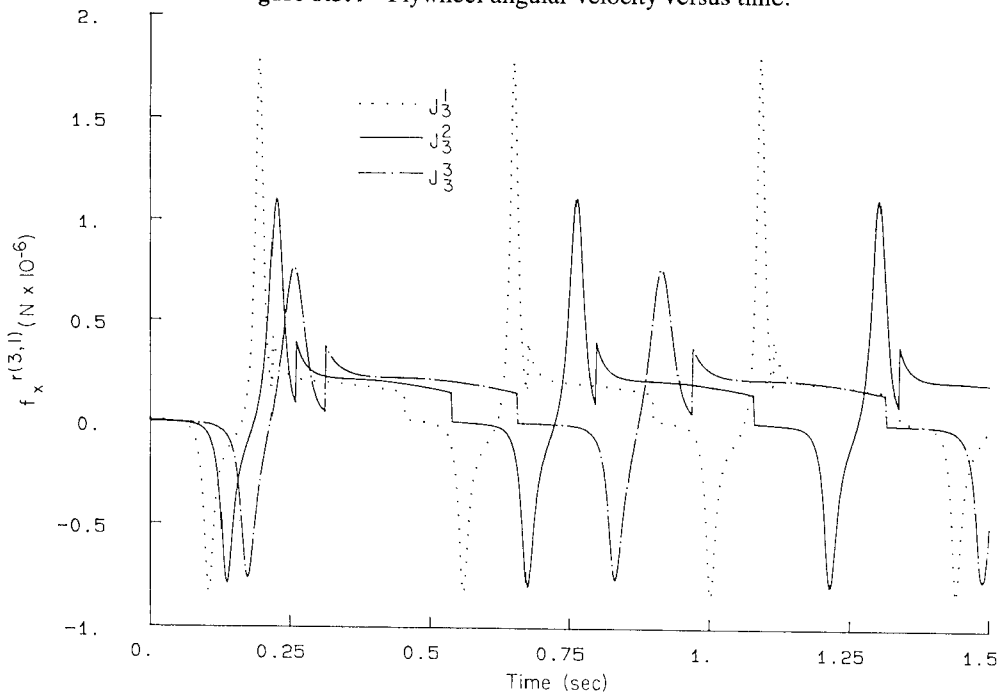

Figure 8.3.5 x-Component of flywheel bearing reaction force versus time.

inertia leads to the lowest cyclic speed, in contrast to the behavior of the compressor of Section 8.2.

Finally, the x component of reaction force between the flywheel and ground, at the revolute joint between bodies 3 and 1, is plotted versus time in Fig. 8.3.5. The greatest variation in this example occurs with the smallest flywheel inertia.

8.4 DYNAMIC ANALYSIS OF A COIL SPRING

In many applications, a relatively long coil spring is used to arrest the motion of a moving body and to return it to its original position. While a coil spring is a continuum of mass distributed along the length of the spring, a reasonable model is formed by discretizing the mass and stiffness of the spring. The lumped mass model shown in Fig. 8.4.1 is constructed by dividing the spring into equal lengths and approximating the mass effects of each component as a lumped mass m. The masses are connected by springs with stiffness k.

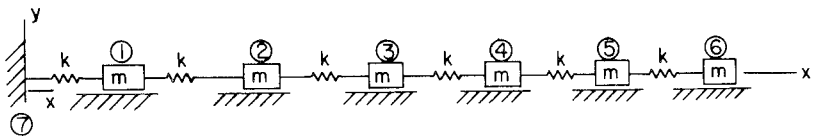

Figure 8.4.1 Model of coil spring.

8.4.1 Surge Waves

To study surge wave behavior, the motion of the system is initiated by giving body 6 an initial velocity in the negative x direction, which might be imparted by impact with another body. The kinematics of the system is defined by prescribing a translational joint between each of the masses and ground, which is body 7. Each spring is attached at the centers of mass of the bodies it connects. The mass of each body is $m = 2.5$ kg, and each spring has the same spring rate $k = 200$ N/m and free length $\ell_0 = 0.2$ m. Therefore, the equilibrium position of body i is $x_i = i \times \ell_0$. Since gravitational force acts in the negative y direction, it has no influence on the motion. The initial velocities of bodies 1 through 5 are zero, and the initial velocity of body 6 is $\dot{x}_6 = -0.1$ m/s, simulating impact on the end of the spring by an external body.

The numerical results of this dynamic simulation include plots of position versus time for each body in Fig. 8.4.2. Note that with even this crude model of wave propagation in the spring, the wave nature of motion, including reflection characteristics at the left end, is accounted for. If a larger number of masses had been used in the simulation, an even closer approximation to actual wave behavior would be produced.

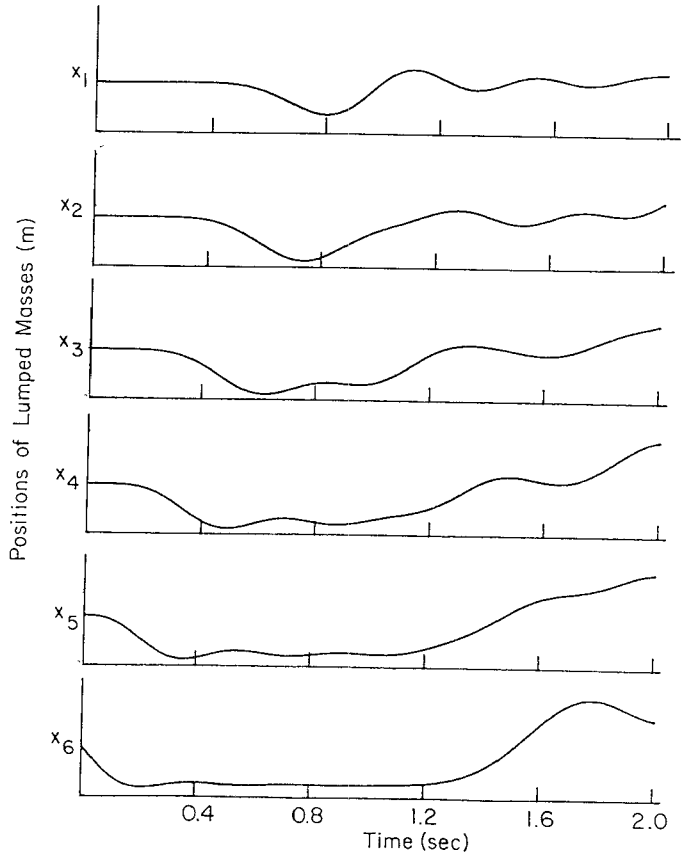

Figure 8.4.2 Lumped mass positions versus time.

8.4.2 Impact and Chattering

In the next application, a heavy mass M (body 8) moves to the left and hits the right end of the spring (body 6), as shown in Fig. 8.4.3. To model the impact between bodies 6 and 8, a unilateral spring with the force-displacement characteristics shown in Fig. 8.4.4 is used. The spring generates no force when its deflection is positive; that is, when bodies 6 and 8 are not in contact. It generates a very large compressive force when the spring deflection is negative; that is, when bodies 6 and 8 are in contact.

For this model, $M = 100\,\text{kg}$, $m = 2.5\,\text{kg}$, $k = 50\,\text{N/m}$, $\dot{x}_8(0) = -0.1\,\text{m/s}$, and all other velocities at $t = 0$ are zero. Figure 8.4.5 shows the resulting positions of the heavy mass and each of the lumped masses as functions of time. Impact occurs as the simulation begins.

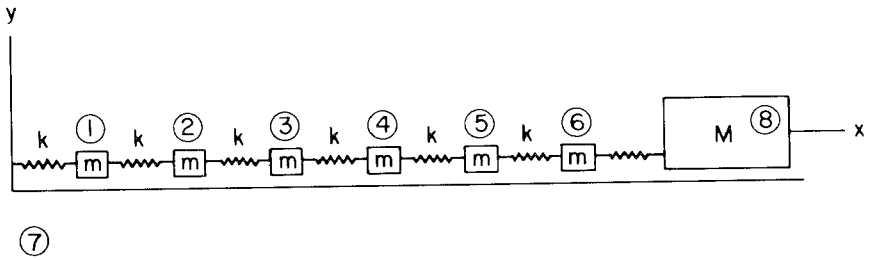

Figure 8.4.3 Model of impact to a long spring.

The maximum displacement Δx_8 of body 8 can be estimated by equating the initial kinetic energy of body 8 to the strain energy of a spring that is equivalent to the six springs in series, that is,

$$\tfrac{1}{2}M(\dot{x}_8)^2 \approx \tfrac{1}{2}k_e(\Delta x_8)^2$$

where $k_e = k/6$. Thus,

$$\tfrac{1}{2}(100)(-0.1)^2 \approx \tfrac{1}{2}(\tfrac{50}{6})(\Delta x_8)^2$$

and

$$\Delta x_8 = \sqrt{6/50} = 0.346 \text{ m}$$

The maximum deflection obtained by dynamic simulation, as shown in Fig. 8.4.5, is $\Delta x_8 = 0.327$ m. The difference is due to the kinetic energy of the lumped masses; that is, when bodies 6 and 8 come to rest, bodies 1 through 5 are still in motion. However, since body 8 is much heavier than the lumped spring masses, the approximation is good.

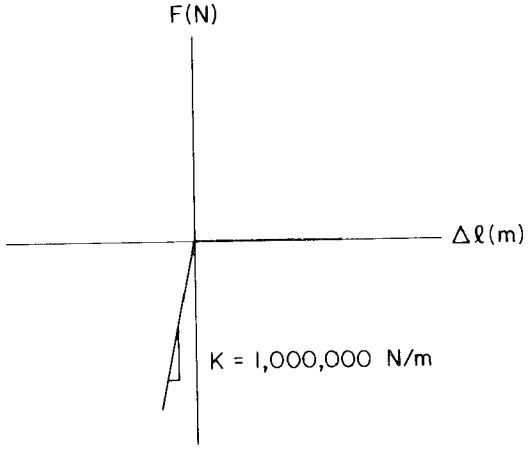

Figure 8.4.4 Unilateral spring characteristic.

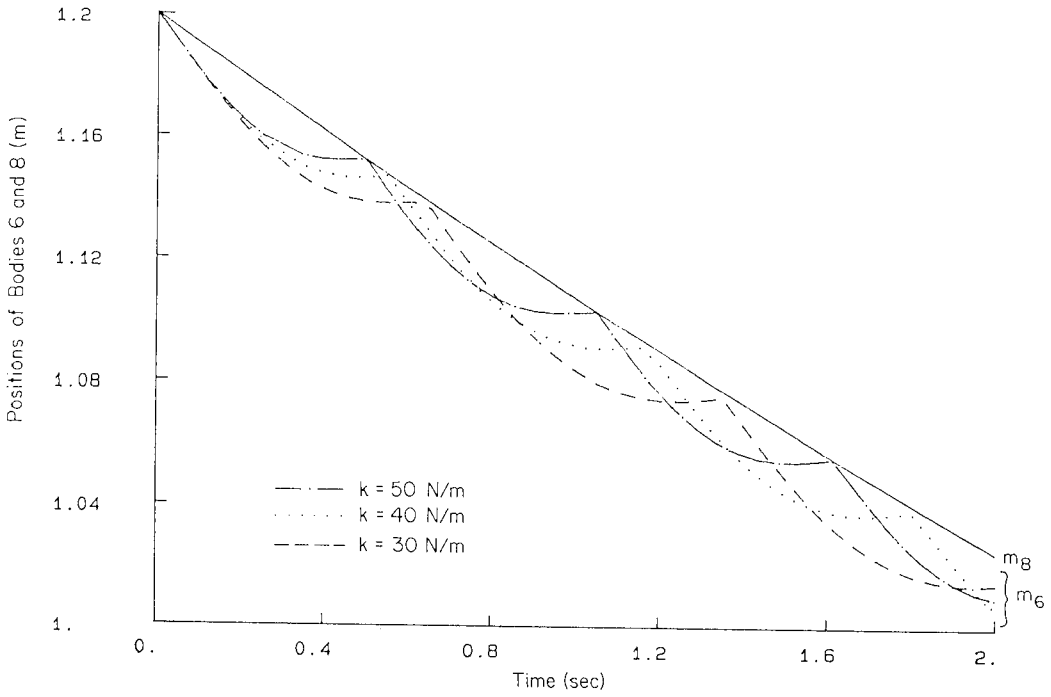

Figure 8.4.8 Chattering between bodies 6 and 8 with no damping.

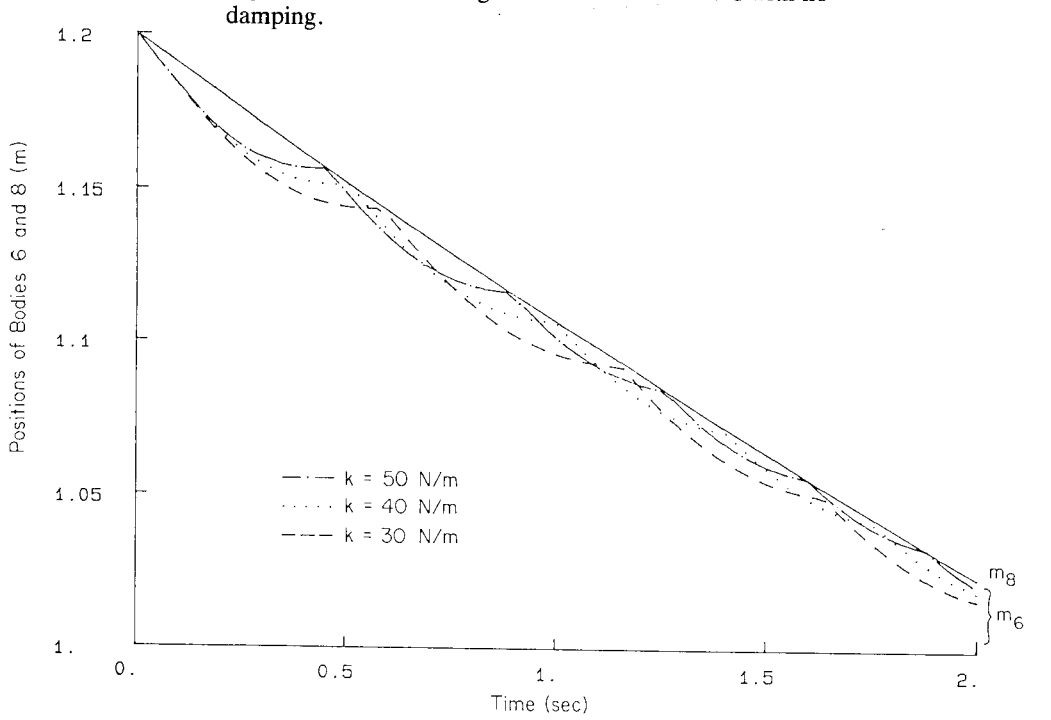

Figure 8.4.9 Chattering between bodies 6 and 8 with damping.

Since the spring between bodies 6 and 8 is very stiff and bilinear, chattering behavior (multiple, high-frequency contacts) occurs between bodies 6 and 8. Bodies 6 and 8 finally separate when $t \approx 11.8$ s, at which time their positions are $x_6 = x_8 \approx 1.27$ m. Since the static equilibrium position is at $x_6 = 1.2$ m, they would separate there if the spring had no mass. However, the spring has a total mass of 15 kg (6×2.5 kg). Hence, it still has kinetic energy when $x_6 = 1.2$, which carries mass 6 beyond $x_6 = 1.2$ m.

Two models, with $k = 40$ and 30 N/m, are simulated, with the results plotted in Figs. 8.4.6 and 8.4.7. The separation time is delayed to 13.4 and 15.3 s, respectively, while the separation position remains approximately the same.

The chattering motion is shown in an expanded time scale in Fig. 8.4.8, which shows the positions of bodies 6 and 8 with $k = 30$, 40, 50 N/m. As k increases, the period of chattering motion decreases, which is due to an increase in wave propagation speed in the spring.

The previous model is now modified to include a unilateral damper between bodies 6 and 8. The logic of the unilateral damper is similar to the unilateral spring in Fig. 8.4.4; that is, no damping force acts when the spring deflection is positive, while a damping force of 200 N · s/$m \times \dot{\ell}$ acts when the spring deflection

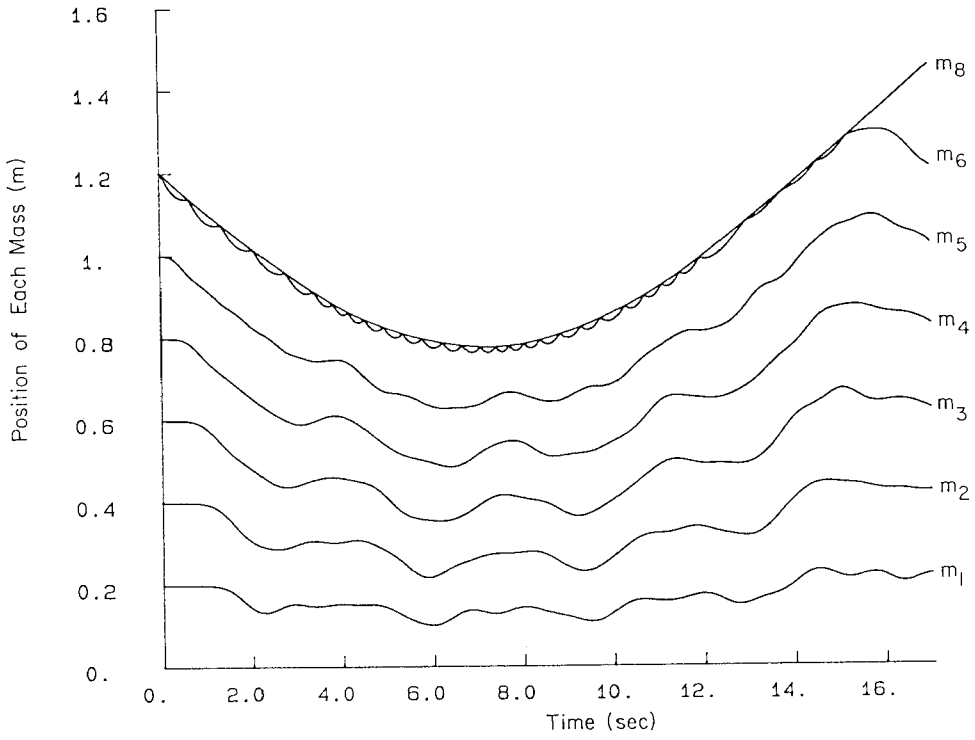

Figure 8.4.7 Chattering and single wave, $k = 30$ N/m.

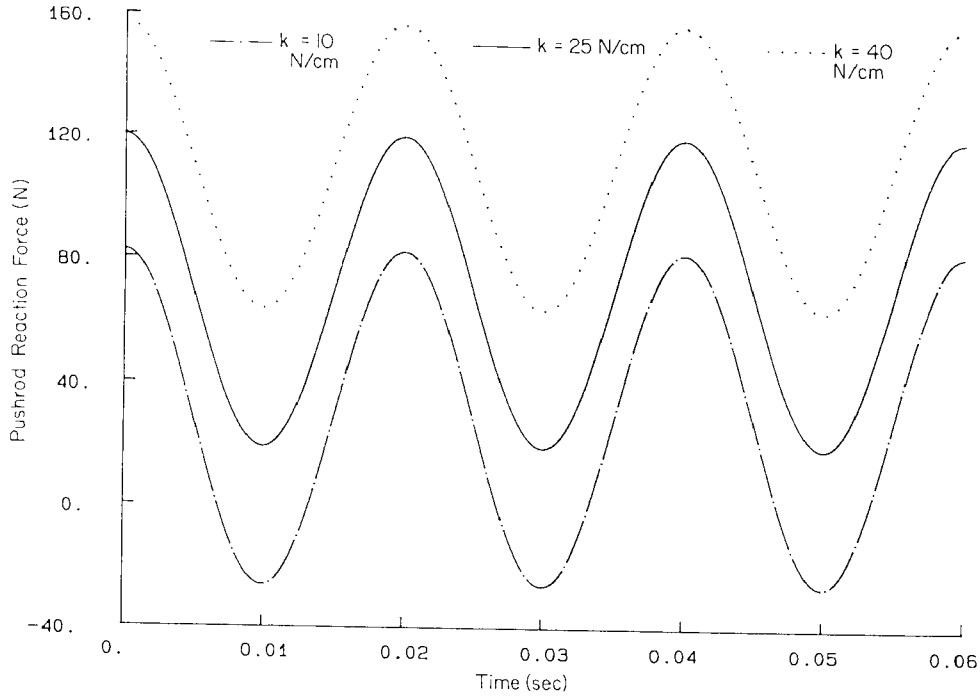

Figure 8.5.1 Pushrod reaction force versus time, 3000 rpm.

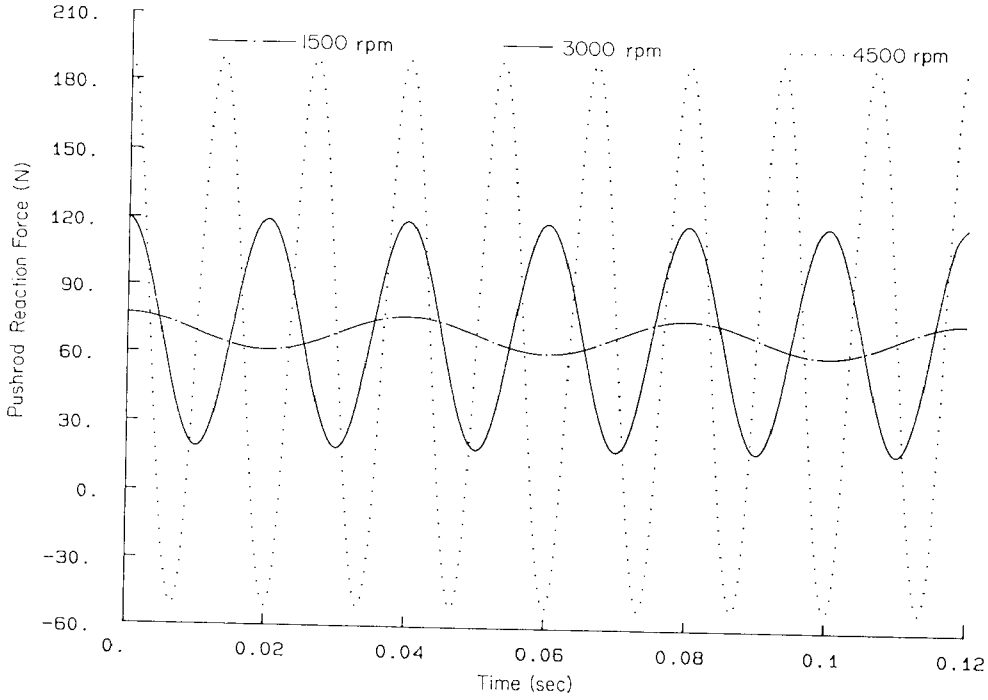

Figure 8.5.2 Pushrod reaction force versus time, k = 25 N/m.

is negative. As shown in Fig. 8.4.9, chattering relative displacement and period are decreased, compared to the case with no damping. It was also observed that the separation position and time remain approximately the same, as in the case with no damping, although plots are not provided.

8.5 DYNAMIC ANALYSIS OF A VALVE-LIFTER MECHANISM

The cam-driven valve mechanism studied in Section 5.6 is analyzed here dynamically. The kinematic model of Section 5.6 is augmented with a valve spring, as shown in the engine of Fig. 1.1.1. Inverse dynamic analysis is carried out to assist in the design of the valve spring.

The masses and moments of inertia of the components of the mechanism of Fig. 5.6.1 are given in Table 8.5.1. The nominal angular velocity of the cam is 3000 rpm (revolutions per minute); that is, 100π rad/s.

TABLE 8.5.1 Mass properties of Valve Lifter Components

Body no.	1	2	3	4	5
Mass (g)	1.0	30.0	120.0	150.0	60.0
Moment of inertia ($g \cdot cm^2$)	1.0	15.0	2250.0	1800.0	800.0

Three runs are made, with varying values of spring constant, $k = 10$, 25, and 40 N/cm. The free length of the spring is 9 cm in each case. Plots of pushrod reaction force with the cam are given in Fig. 8.5.1.

With $k = 10$ N/cm, a negative reaction force occurs between the pushrod and the cam at about $t = 0.01$ s, when the pushrod reaches its highest point. This is due to the inertia of the parts. In an actual cam–flat-faced follower, separation would thus occur. Since the formulation of the cam–flat-faced follower joint does not allow separation, the reaction force appears to be negative. This unacceptable behavior can be corrected by increasing the spring constant of the valve spring. As seen in Fig. 8.5.1, with $k = 25$ and 40 N/cm, the negative reaction force does not appear. These designs would, therefore, be acceptable at 3000 rpm.

Three more runs are made with the nominal spring constant $k = 25$ N/cm and cam speeds of 1500, 3000, and 4500 rpm. Plots of pushrod reaction force are shown in Fig. 8.5.2. With 1500 and 3000 rpm, negative reaction force does not occur. However, at 4500 rpm the reaction force becomes negative. Hence, 4500 rpm is not an acceptable operating speed for a valve spring with $k =$ 25 N/cm.

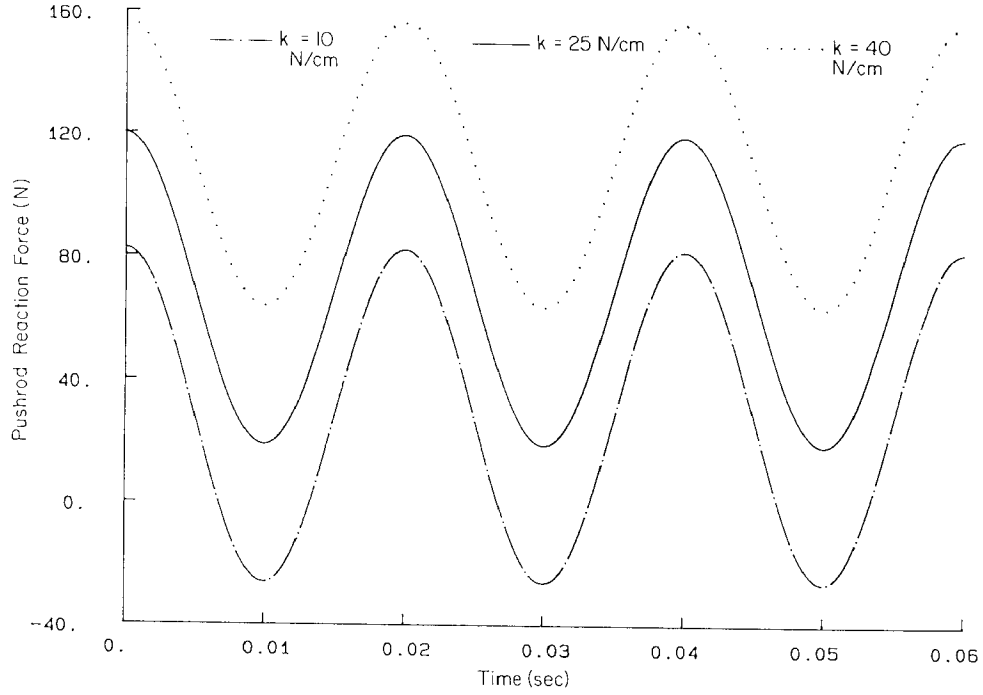

Figure 8.5.1 Pushrod reaction force versus time, 3000 rpm.

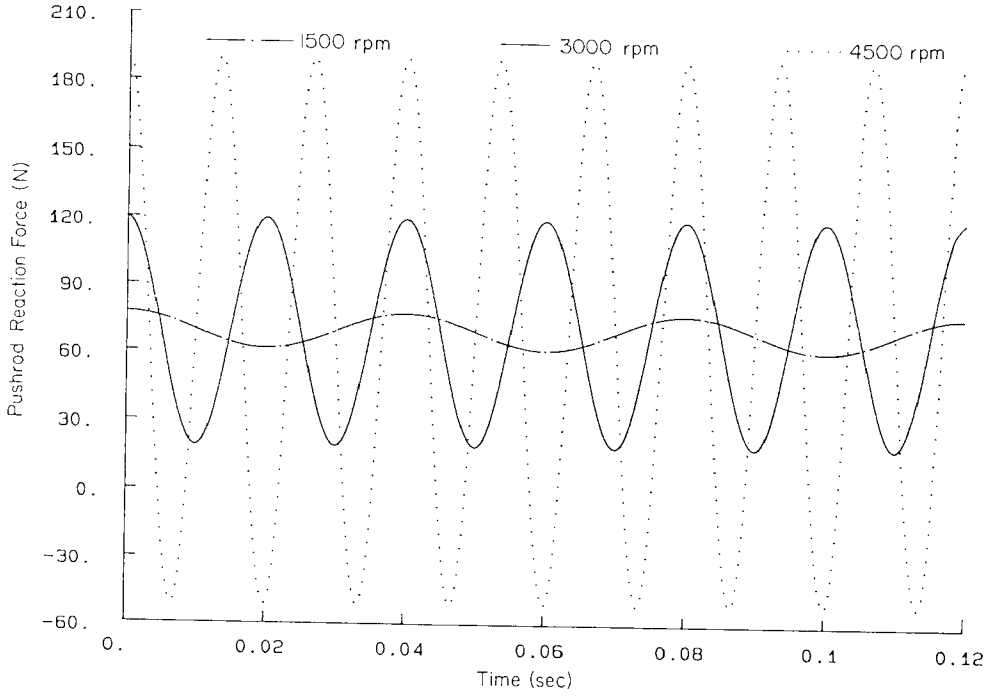

Figure 8.5.2 Pushrod reaction force versus time, k = 25 N/m.

DADS PROJECTS

8.1. Perform a dynamic analysis of the film follower of DADS Project 5.1 using additional data as follows:

Inertial Properties of Bodies

Body	Mass (kg)	Polar Moment of Inertia ($kg \cdot m^2$)	Centroid
1	1.0	1.0	0.0
2	0.0012	2.25×10^{-8}	Midpoint of AB
3	0.01	9.2×10^{-8}	50 from B
4	0.0025	4.5×10^{-8}	Midpoint CD

The reader must be reminded that the body-fixed frames need to be redefined for dynamic analysis. Consider a few ways to drive the mechanism dynamically. One suggestion is to apply a torque to crank AB.

8.2. Perform a dynamic analysis of the web cutter of DADS Project 5.2 using additional data as follows:

Inertial Properties of Bodies

Body	Mass (kg)	Polar Moment of Inertia ($kg \cdot m^2$)	Centroid
1	1.0	1.0	0.0
2	0.1	1.5×10^{-5}	Midpoint of AB
3	1.0	0.03	C
4	2.0	0.04	(0.14, 0.07) with respect to x_4'-y_4' of DADS Project 5.2

For the definition of body-fixed frames and driving method, refer to DADS Project 8.1.

8.3. Perform a dynamic analysis of the rack and pinion mechanism of DADS Project 5.3. The masses of the pinion, rack, and coupler are 0.05, 0.1, and 0.05 kg, respectively. Redefine the body-fixed frames and apply torque for dynamic analysis. An alternative model can be constructed by replacing the coupler with a revolute–revolute joint.

8.4. Perform an inverse dynamic DADS analysis for the slider–crank mechanism of Section 8.2. Obtain the constraint reaction torque for the kinematic driver used. Use the resulting torque information as an applied torque to perform a dynamic DADS run and compare the results.

8.5. Perform inverse dynamic and dynamic runs for the quick-return mechanism of Section 8.3.

Part Two

SPATIAL SYSTEMS

Chapters 9 through 12 are devoted to Cartesian kinematics and dynamics of systems in which all bodies move in space. Many of the basic concepts needed have been developed in Part One. Extension of the mechanical system analysis from the planar to the spatial setting, however, requires the introduction of three-dimensional vector analysis and, of particular importance, analysis of the orientation of a body in space. The matrix, vector calculus, and numerical methods developed in Part One are adequate in almost all respects for the treatment of spatial systems.

Chapter 9 begins with an extension of vector analysis to the spatial setting and provides a self-contained treatment of the rotation and orientation of bodies in space. Angular velocity and virtual rotation are introduced and illustrated in preparation for the development of a unified theory of spatial kinematics. Euler parameter orientation coordinates are introduced and their properties are developed to support spatial kinematic and dynamic analysis. The remainder of Chapter 9 presents a spatial kinematic constraint formulation that parallels the developments presented in Chapter 3 for planar systems. Since the numerical methods for spatial kinematics are identical to those for planar kinematics, the numerical methods of Chapter 4 need not be repeated for spatial applications.

Chapter 10 is devoted to modeling and analysis methods for spatial system kinematics. Of particular importance in spatial kinematic analysis is model definition, using an extensive library of kinematic couplings that occur in spatial kinematics. Numerical examples are presented to illustrate the difficulties that can be encountered in modeling. Guidelines are presented to assist the engineer in proper model selection and analysis.

Spatial equations of motion for a single rigid body and for multibody systems are derived in Chapter 11, including the inertia properties of bodies and a variational form of the equations of motion. The basic development is identical in form to that presented in Chapter 6 for planar systems, with the exception that nonlinear terms associated with angular velocity arise in the spatial case. Equations of motion are formed in terms of both angular velocity and Euler parameter generalized coordinates. Numerical integration methods for equations of motion in Euler parameter generalized coordinates are identical to

those presented in Chapter 7. Some modifications in integration methods, to exploit the angular velocity form of equations of motion, are presented. Finally, Chapter 12 presents applications of the Cartesian dynamics formulation to assist the reader in gaining experience and confidence in using the methods.

The reader is cautioned that the analytical and algebraic complexity of spatial system kinematic and dynamic analysis is substantially greater than has been experienced in the study of planar systems in Part One. To achieve a practical capability in spatial system kinematic and dynamic analysis, the engineer must master the basic concepts of three-dimensional vector analysis and the use of generalized coordinates to define the position and orientation of bodies in space. While the algebra and calculus of these methods may appear to be complicated, they are easily understood if the reader builds on the intuitive concepts of planar kinematic and dynamic analysis developed in Part One. A combined analytical and physically intuitive approach to spatial system kinematics and dynamics can aid immeasurably in understanding what might otherwise be viewed as abstract mathematical manipulations.